Materials Advances

ROYAL SOCIETY OF CHEMISTRY

PAPER

View Article Online
View Journal | View Issue

Cite this: *Mater. Adv.*, 2023, 4, 256

Classical nexus between chiral inducers and achiral silver nanoparticles and integration of the digital XOR logic gate†

Manajit Mandal, Ankur Malik and Prakash Chandra Mondal *

Chirality-induced metallic and metal–oxide nanoparticles (NPs) hold promising potential in chiroptical activity, asymmetric catalysis, chiral discrimination, and drug delivery. Herein, we report a simple but scalable method for the preparation of achiral, metallic colloidal Ag NPs in which chirality was imprinted using organic chiral inducers. Chirality can be imprinted into Ag NPs upon surface functionalization using L- and D-cysteine. The formation of nanostructure assemblies, morphology, and chemical compositions are ensured by electron microscopy (TEM, FE-SEM) and X-ray photoelectron spectroscopy (XPS). Amino acid-driven enhanced chiroptical activity, followed by anisotropy factors (*g*-factor) of the Ag core and thiolate adsorbates were investigated by CD spectroscopy. Strong chiroptical activity in cysteine-modified Ag NPs originates from metal-based interband electronic transitions (as transitions are highly energetic), which is absent in free chiral inducers. Considering the chiral ligands, individual or combined use for Ag NP surface modification as chemical inputs and CD signal as an output, an XOR logic gate was implemented. L-Cys@Ag and D-Cys@Ag NPs are integrated into electronic devices for DC-based electrical measurements (current–voltage, *I*–*V*) and AC-based electrical impedance spectroscopy (EIS) for deducing individual electrical components, followed by equivalent circuit modeling. The conductivity of the L-Cys driven-Ag NPs assembly decreases compared to the D-Cys Ag-NPs assemblies, thus ensuring a higher degree of Ag NPs surface modification than the former chiral inducer. The present work enriches the facile synthesis of chiral NPs and large-scale electrical devices that can be envisioned for chirality-driven photocatalysis, optoelectronic devices, bio-sensing, and molecular spintronics.

Received 30th September 2022,
Accepted 18th November 2022

DOI: 10.1039/d2ma00942k

rsc.li/materials-advances

1. Introduction

'Structure defines properties' is a compelling statement appropriate in chemistry, materials science, biology, and engineering. It is true that when the dimension of noble metals or metal–oxides is reduced to nanoscale size (diameter ~1–100 nm), they show many striking optical and electronic properties, which are well-celebrated phenomena at the nanoscale.[1–5] Their size-dependent optoelectronic properties differ to a great extent from their respective bulks as nanomaterials show high surface area over volume ratio and quantum confinement of charge carriers at the nanoscale.[6,7] Although gold (Au) nanoparticles such as Au_{34} cluster show inherent chirality, their *g* valves are extremely low and do not serve practical purposes.[8–11] A simple but effective way to convert achiral metallic or semiconducting nanomaterials into chiral is using a chiral precursor, an icing on the cake. Chirality, an important property that can be found in many compounds, is significant in biochemistry, pharmacy, and spin-filtering phenomena.[12–15] However, an excellent nexus between nanoparticles and chiral ligand is a must, not only to imprint chirality but to control the growth of nanomaterials and degree of surface functionalization. Recently, chiral inorganic materials have gained considerable attention due to their unique chiroptical activity and applications in many fields, for *e.g.*, chiral catalysis, chiral (or helical) supramolecular assemblies, optical, chiral discrimination, sensing, and drug delivery.[16–21] Chirality in inorganic materials, especially plasmonic metallic nanoparticles, can emerge due to inherent asymmetrical geometry or induction of chirality by naturally occurring organic chiral molecules.[22–25] The enhancement of chiroptical property in chiral ligand-linked nanomaterials due to the electronic transitions (interband and intraband) is related to the non-zero dot product of electric and magnetic dipole transition

Department of Chemistry, Indian Institute of Technology Kanpur, Uttar Pradesh 208016, India. E-mail: pcmondal@iitk.ac.in

† Electronic supplementary information (ESI) available: Temperature and concentration dependence UV-vis spectra; temperature-dependence CD spectra; FE-SEM images, DLS size distribution; expended and deconvoluted spectra of C 1s and N 1s, FT-IR and Raman spectra, optical rotation values, current density *vs.* potential (*J*–*V*) plots of reference devices, video file of XOR logic gate. See DOI: https://doi.org/10.1039/d2ma00942k

moments.[10,26,27] To control the surface morphology, size, reactivity, and shape of nanoparticles by introducing inherent chirality is a challenging task; however, efforts have been made to overcome these obstacles.[28–31]

Chirality induction into achiral metallic nanomaterials has received increasing attention because the method offers the ability to achieve strong optical activity over a broad spectral range.[9,32,33] Since the first report on the formation of chiral gold nanoparticles in the year 2000 by Schaaff and co-workers, the domain has flourished incredibly.[34] However, gold (Au) NPs are widely employed to imprint chirality into them, using the chirality-grown mechanism, followed by a wide range of applications.[18,35–38] However, silver (Ag) NPs are relatively unexplored in terms of chirality induction, which could be due to that fact that its reactivity is difficult to control at the nanoscale. Considering its abundance and inexpensiveness, as compared to Au, the development of chiral Ag nanoparticles *via* a reasonable and cost-effective approach can be an attractive additive for the fabrication of heterostructured memory devices and nanotechnological applications, provided controlled growth technique is accomplished.[39] Recently, few groups have employed different synthesis platforms (Turkevich method, microwave-assisted, ultrasonication) to prepare either L or D or L- and D-cysteine-modified Ag NPs for studying chiroptical properties, chiral amino acids, and biological fluids sensing.[40–43] However, the electrical properties of chiral assemblies are almost untouched, and chiral-induced growth is uncontrolled. Thus, there is a pressing need for using them as circuit elements in electronic devices and understanding the current–voltage relationship as it is vital for real applications, besides achieving controlled growth *via* a feasible chemical method.

Herein, we report a facile two-step approach for the preparation of L- and D-cysteine-modified chiral Ag NPs *via* surface modification. Several parameters, such as the concentration of L-/D-Cys and effect of temperature, were investigated using UV-vis and CD spectroscopy measurements. Based on CD intensity as the output signal, and L-Cys (Input1), D-Cys (Input2), an XOR logic gate was integrated. Such mimicking is vital to build nanomaterials-based transistors. Electrical measurement experiments such as *I–V* measurements and solid-state electrical impedance spectroscopy followed by circuit modelling were performed and relation with the degree of functionality with the chiral ligand was established.

2. Results and discussion

Synthesis

Polydisperse silver nanoparticles were synthesized by borohydride reduction of $AgNO_3$ in presence of tri-sodium citrate (TSC) and polyvinylpyrrolidone (PVP) K-30 (Fig. 1). L-Cys@Ag and D-Cys@Ag were obtained by the functionalization of Ag NPs using chiral L-Cys and D-Cys. Detailed synthetic procedures can be found in the experimental section. We performed this reaction at least 20 times and could be able to find the similar results in 18 cases (~90% reproducibility), and non-reproducible results were obtained due to the oxidation of Ag NPs. However, the variation in the respective data is also mentioned during its description. Morphology and chemical compositions were studied by field-emission scanning electron microscopy (FE-SEM), transmission electron microscopy (TEM), and X-ray photoelectron spectroscopy (XPS). Circular dichroism (CD) spectroscopy was employed to study the chiroptical properties of L-Cys@Ag and D-Cys@Ag NPs. Once the Ag NPs were modified with the chiral ligands, they were integrated into solid-state devices for both DC and AC electrical measurements using the two-probe contact method.

Morphology and chemical composition

The spherical shape of Ag nanoparticles can be observed in the TEM images of unmodified AgNPs, L-Cys@Ag, and D-Cys@Ag NPs (Fig. 2(a)–(c)), and the average particles size of AgNPs was calculated with the help of ImageJ software; the values were 16.9 ± 0.3 nm, 16.6 ± 0.5 nm, and 16.4 ± 0.4 nm, respectively (see inset of

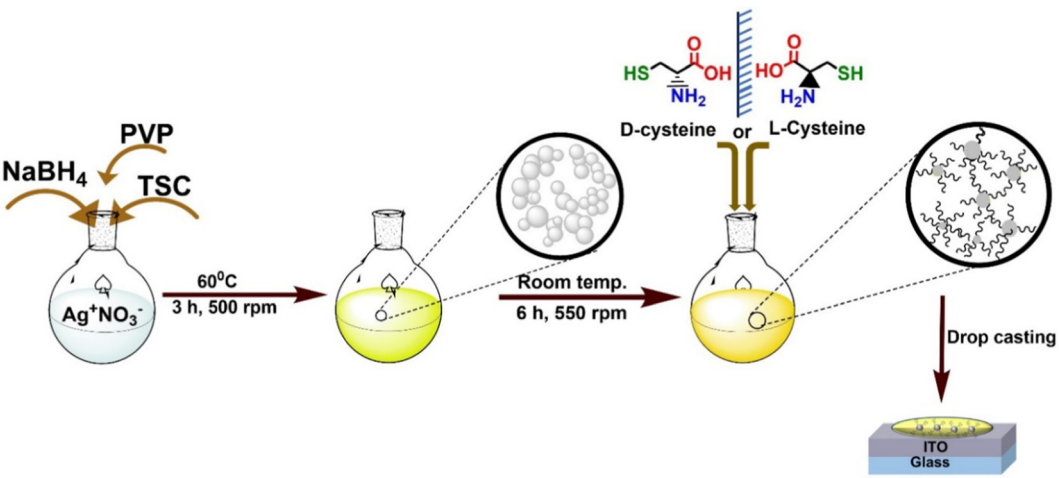

Fig. 1 Synthetic scheme for the preparation of Ag NPs, followed by imprinting chirality into Ag NPs by L/D-cysteine used for chiroptical and DC and AC-based electrical measurements on drop-casted films deposited on ITO.

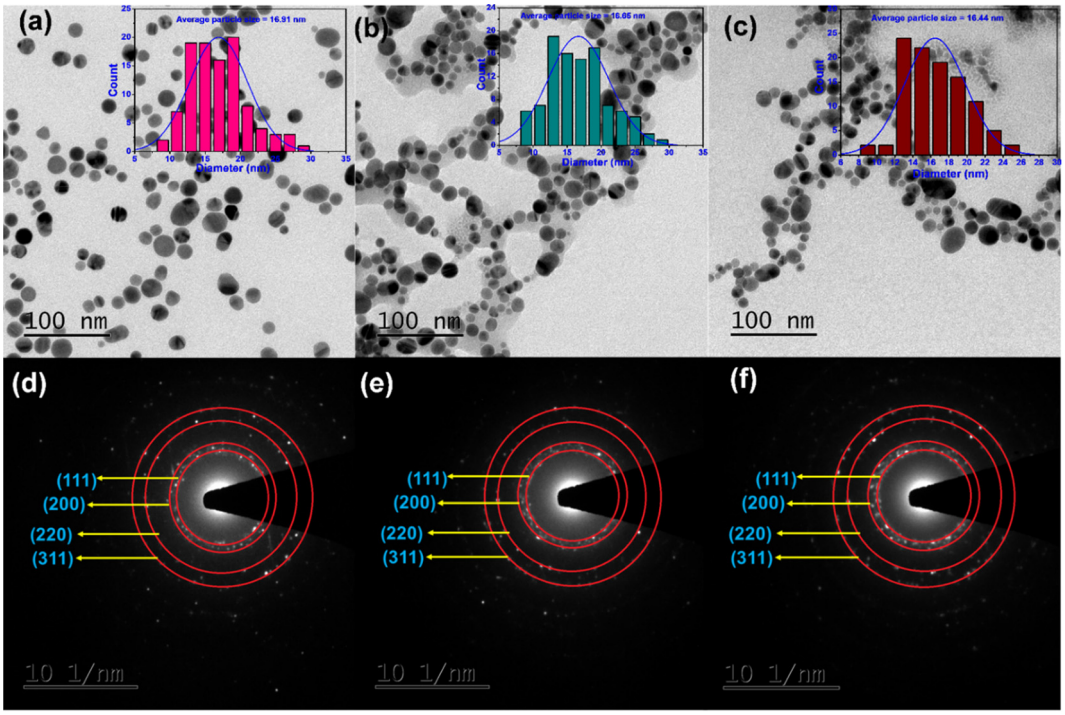

Fig. 2 TEM images of (a) unmodified Ag NPs, (b) L-Cys@Ag, and (c) D-Cys@Ag (particle size distributions (counts *vs.* diameter) shown in inset), and corresponding selected area electron diffraction (SAED) pattern of (d) Ag NPs, (e) L-Cys@Ag, and (f) D-Cys@Ag NPs, respectively.

Fig. 2(a)–(c)). This result ensures that the chiral ligand modifications do not alter the size of the Ag NPs, which ensures stability and control of reactivity, *i.e.*, no agglomeration was found during the process of chirality transfer. In the selected area electron diffraction (SAED) pattern of unmodified AgNPs, L-Cys@Ag, and D-Cys@Ag NPs, concentric rings corresponding to the (111), (200), (220), and (311) planes of Ag-*Syn* (JCPDS-00-04-0783) were observed, indicating the polycrystalline nature of Ag NPs (Fig. 2(d)–(f)). L-Cys@Ag and D-Cys@Ag NPs show intertwisted flower-like morphology, as can be seen in the FE-SEM images (Fig. S1c–f, ESI†); more TEM images are provided in Fig. S1a and b (ESI†). To determine the particle size, dynamic light scattering (DLS) measurements were employed, and it eas found to be 14.9 ± 0.3 nm, 16.2 ± 0.3 nm, and 15.4 ± 0.5 nm for AgNPs, L-Cys@Ag, and D-Cys@Ag NPs, respectively (Fig. S2, ESI†), which are in good agreement with the TEM results. Such minor variation may occur from different batches of sample preparation. A decrease in the zeta potential as compared to the unmodified Ag NPs was observed. For instance, the zeta potentials were measured at −25.3 ± 2 mV and −29.5 ± 1.5 mV, −27.9 ± 1.8 mV for pristine Ag NPs, L-Cys@Ag, and D-Cys@Ag NPs, respectively, demonstrating the formation of stable colloidal particles even after the functionalization of Ag NPs with chiral ligands. A similar observation was made with the hydroxylamine-modified colloidal Ag NPs.[44]

FT-IR and Raman studies

Formation of covalent interfaces at Ag NPs and sulphur of L/D-Cys in L-Cys@Ag NPs and D-Cys@Ag NPs were confirmed by FT-IR spectroscopy (Fig. S3a, ESI†). ATR-FTIR spectra were recorded in the range of 4000–600 cm^{-1} and the band observed at 2540–2550 cm^{-1} for pure L/D-Cys corresponded to S–H stretching frequency.[45] The above band was absent in the case of either L-Cys@Ag or D-Cys@Ag NPs, unequivocally indicating the formation of Ag–S bonds. This is not surprising due to the soft–soft interaction between the thiols of L/D-Cys and Ag NPs that prefers to make a covalent bond over the possibilities of Ag–NH_2 or Ag–O bond formation. A high intensity signal in the frequency range of 3000–3600 cm^{-1} is attributed to N–H stretching merged with –OH deformation. A weak signal observed at 1638 cm^{-1} corresponds to C═O stretching, attributed to the carbonyl of carboxylic acids. Aromatic C–H stretching observed at 3030 cm^{-1} was merged with N–H stretching. Raman spectra were recorded in the liquid state, where the free $-NH_3^+$ of one L/D-Cys molecule combined with the COO^- end of another L/D-Cys through H-bonding, which was confirmed by Raman spectra as the peaks corresponding to $-COO^-$ and $-NH_2$ at 1400 cm^{-1} and 1067 cm^{-1}, respectively, were absent (Fig. S3b and c, ESI†). A peak at 1090 cm^{-1} for C–N was observed, confirming no direct interaction between Ag NPs and the NH_2 group of L/D-Cys.[45,46]

X-Ray photoelectron spectra (XPS)

The deconvoluted XPS spectra of Ag 3d of pristine Ag NPs, L-Cys@Ag, and D-Cys@Ag NPs are depicted in Fig. 3(a)–(c) (ESI†), and the full scan survey spectrum is shown in Fig. S4 (ESI†). All the peaks (binding energies) were calibrated with reference to the C 1s signal at 284.5 eV. The full scan survey spectrum of Ag NPs shows the presence of metallic silver, and that of L-Cys@Ag

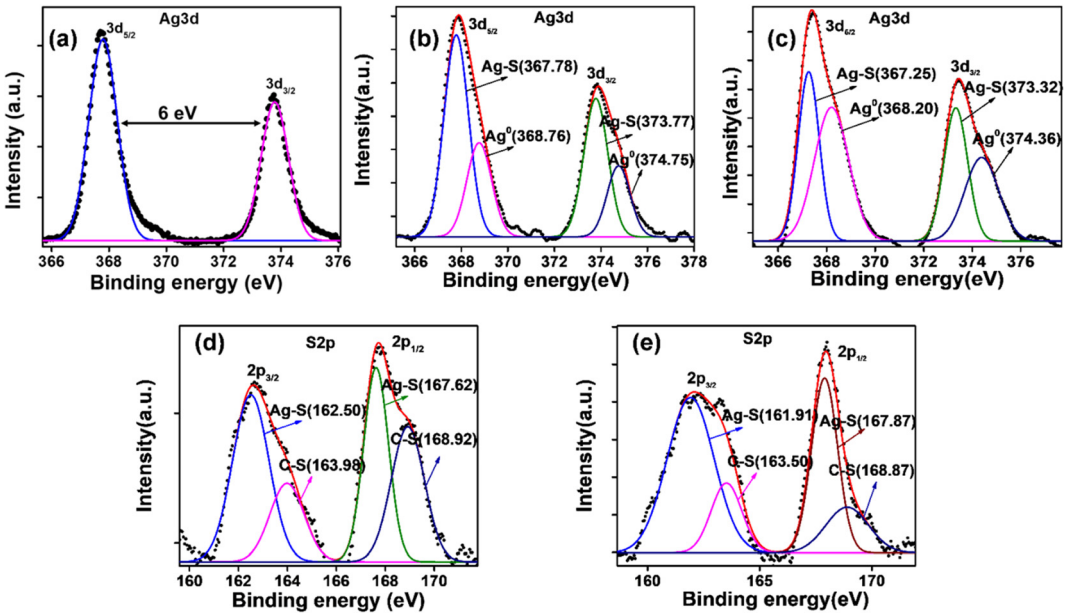

Fig. 3 XPS spectrum of Ag 3d of (a) pristine Ag NPs, (b) L-Cys@Ag NPs, (c) D-Cys@Ag NPs, (d) and (e) expended and deconvoluted spectra of S 2p of L-Cys@Ag NPs and D-Cys@Ag NPs, respectively.

and D-Cys@Ag NPs shows the presence of Ag, C, N, S, and O at their respective binding energies. The binding energies of different electronic states of the elements of Ag NPs, L-Cys@Ag, and D-Cys@Ag NPs are provided in Table S1 (ESI†). The high intensity peaks at 367.30 eV and 373.30 eV due to Ag $3d_{5/2}$ and Ag $3d_{3/2}$ were observed in Ag NPs, while lower intensity peaks of Ag $3d_{5/2}$ and Ag $3d_{3/2}$ in L-Cys@Ag and D-Cys@Ag NPs were observed at 367.86 eV and 373.87 eV, and 367.44 eV and 373.44 eV, respectively.[47] The peaks with moderate intensity at 162.61 eV and 162.08 eV were corresponding to S $2p_{3/2}$ in L-Cys@Ag and D-Cys@Ag NPs. N 1s was observed at 399.60 eV and 399.55 eV, and O 1s was seen at 530.80 eV and 530.50 eV in L-Cys@Ag and D-Cys@Ag NPs, respectively. The expanded and deconvoluted spectra of S 2p of L-Cys@Ag and D-Cys@Ag NPs is given in Fig. 3(d) and (e). The deconvoluted spectra of C 1s and N 1s of L-Cys@Ag and D-Cys@Ag NPs are given in Fig. S5 (ESI†). The XPS results confirm the formation of L- and D-Cys-capped Ag NPs.

Polarimetry

Polarimetric study of pure solution of free chiral ligands and capped Ag NPs was performed at room temperature (298 K) to explore the chirality enhancement. For instance, the optical rotation of 5 mM L-Cys and L-Cys@Ag was observed at −0.003 degree and −0.030 degree, respectively. Similarly, the optical rotation of 5 mM pure D-Cys and D-Cys@Ag was 0.002 degree and 0.019 degree, respectively, indicating a 10-fold increase in the optical rotation of free chiral ligands upon interacting with the Ag NPs, ensuring an upsurge in the chiroptical activity. The optical rotation values are summarized in Table S2 (ESI†). The above results support the shifting and intensification of the CD spectra data in both L- and D-Cys@Ag NPs, as discussed below.

Optical and chiroptical studies

Chirality in any object is caused by a non-zero numerical function of the dot product of magnetic dipole moment transition (m) and electric dipole moment transition (μ), given by Rosenfeld equation, $R = \mathrm{Im}(m \cdot \mu)$, where R represents the CD intensity at a given transition and Im is the imaginary section of the scalar product.[48] A broad absorption band at 396 nm was observed in the UV-vis spectrum of freshly prepared Ag NPs corresponding to surface plasmon resonance (SPR) phenomenon (Fig. 4(a)), which matches well with a previous report.[49] The intensity of the SPR band is drastically decreased after the functionalization of Ag NPs with L/D-Cys chiral molecules, and there was no change in the λ_{max}, indicating that the band originated from Ag SPR in L/D-Cys@Ag NPs; thus, the possibility of agglomeration can be ruled out. The functionalization by L/D-Cys in L/D-Cys@Ag NPs blocks the direct absorption of light photons, thus reducing the SPR population and band intensity. The absorbance of L-Cys@Ag is slightly lower than that of D-Cys@Ag; this may be due to the slight variation in the surface coverage of Ag NPs caused by the experimental conditions.[43] Temperature-dependent UV-vis analysis was performed in the range of 25–80 °C at an increment of 5 °C. The result showed that there was no significant change in the absorbance value and λ_{max}, indicating that the chiral assemblies are stable up to atleast 80 °C (Fig. S6, ESI†). We further employed circular dichroism (CD) spectroscopy, which is a very useful technique for the characterization of chiroptical properties.[50,51] A controlled experiment performed with L/D-Cys (racemic mixture)-capped AgNPs showed a flat line in the CD signal due to the nullified chiroptical behavior of AgNPs (Fig. S7a, ESI†). The concentration of Ag NPs was kept fixed at 5 mM, while the concentration of L/D-Cys was varied as 0.1, 0.5, 1, 5 and 10 mM

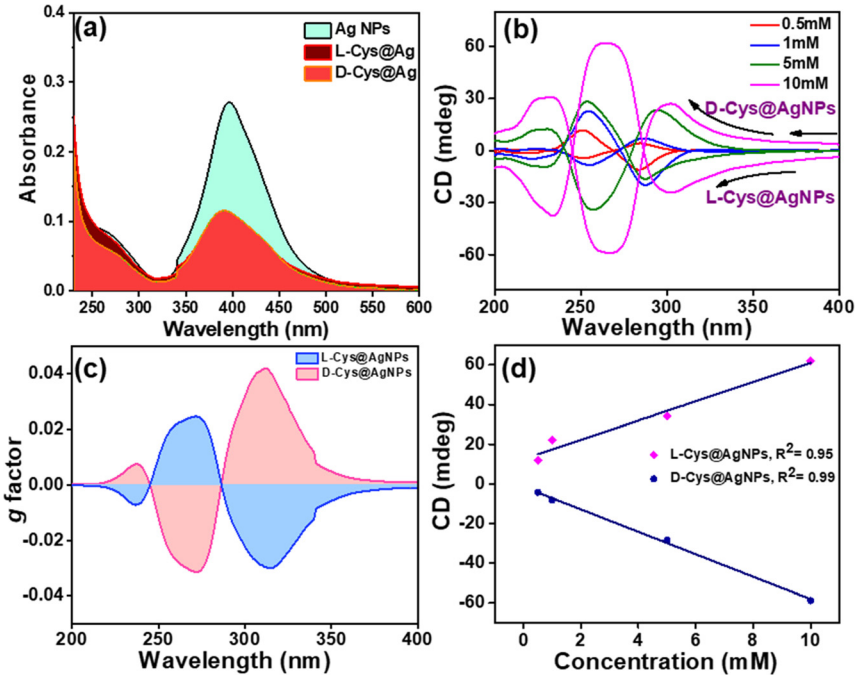

Fig. 4 (a) Comparison of the UV-vis spectra of Ag NPs, L-Cys@Ag, and D-Cys@Ag, (b) comparison of the CD spectra at various concentrations of L/D-Cys, (c) *g*-factor plot at 5 mM concentration of L/D-Cys, and (d) plot of ellipticity (mdeg) *vs.* concentration of chiral ligands (L, D-Cys) added to Ag NPs.

for CD measurements (Fig. 4(b)). The intensity of the CD signal increased regularly as the concentration of the L/D-Cys increased from 0.1 mM to 10 mM in the UV range of 240–360 nm. The CD signal of L/D-Cys@Ag NPs showed that at low concentration of L/D-Cys, they were not perfect mirror images of each other (Fig. 4(b)), which was also evident from the very low values of *g*-factor (0.006, 0.01, and 0.02) at lower concentrations (0.5 mM, 1 mM, and 5 mM) of L/D-Cys. A red shift due to the higher concentration of the chiral ligand is attributed to the stronger interaction among the chiral NPs. The maximum anisotropy factor or *g*-factor was calculated for L/D-Cys@Ag NPs prepared using 10 mM of L/D-Cys as chiral inducer organic ligand and was found to be 0.04 (Fig. 4(c)). The *g*-factor was calculated using the following equation

$$g = [2(A_L - A_R)]/(A_L + A_R)$$

where, A_L and A_R indicate absorbance of left and right circularly polarized light, respectively. Fig. 4(d) reveals a plot of concentration *vs.* ellipticity (mdeg), which follows the linear trend with R^2 value of 0.95 for L-Cys@Ag and 0.99 for D-Cys@Ag NPs. The plasmonic CD signals of L-Cys@Ag and D-Cys@Ag NPs are known to be strongly temperature-dependent. The temperature-dependent CD spectra show that with an increased temperature, the CD intensity decreased regularly in both L-Cys@Ag and D-Cys@Ag NPs (Fig. S7b, ESI†). A plot of temperature *vs.* CD (mdeg) is presented in Fig. S7c (ESI†), which also followed a linear trend (R^2 = 0.99) with a negative slope of −0.15 for L-Cys@Ag NPs and −0.18 for D-Cys@Ag NPs, suggesting that the rate of decrease in the CD intensity for D-Cys@Ag NPs is higher that of L-Cys@Ag NPs. It seems that CD induction is largely produced by the electromagnetic or dipole coupling mechanism.[52] Pure chiral inducers L/D-Cys show a CD signal at about 190–240 nm, and the same was performed upon increased concentration of each chiral inducers but in the absence of Ag NPs (Fig. S7d, ESI†), which are entirely different from that of capped Ag NPs.

Integration of exclusive OR Logic gate

Logic gates are the heart of integrated circuits (ICs). For example, IC 7486 consists of four XOR logic gates. Therefore, it would be exciting to mimic the XOR logic gates employing the L-Cys@Ag and D-Cys@Ag NPs and understand their logic gate behavior. It can be demonstrated that Ag NPs can simulate the XOR logic function based on the response profiles of ellipticity in terms of the CD signal. A XOR gate is a two-input device with its output signal in the "on-state" when the input strings are "10" and "01", and in the "off-state" when the input strings are "00" and "11". In our case, to implement XOR logic gates, L-Cys and D-Cys are considered as Input1 (A = In1) and Input2 (B = In2), respectively, while the CD intensity is considered as an output (Out1). From the above chiroptical studies, it is evidenced that in the absence of L/D-Cys, Ag NPs do not show enhanced CD signal; thus, Out1 would be zero ("0"). On the other hand, either L-Cys or D-Cys can enhance the CD signal; thus, the corresponding Out1 would be one ("1") for both the cases. Interestingly, when both the chiral inducers were added simultaneously with equivalent molar, they cancelled each other, and the resultant Out1 would be zero (0). The molecular level logic gate is implemented here based on the individual and combined usages of chiral inducer, L- and D-Cysteine. We consider the CD signals of 5 mM concentrations of either Ag

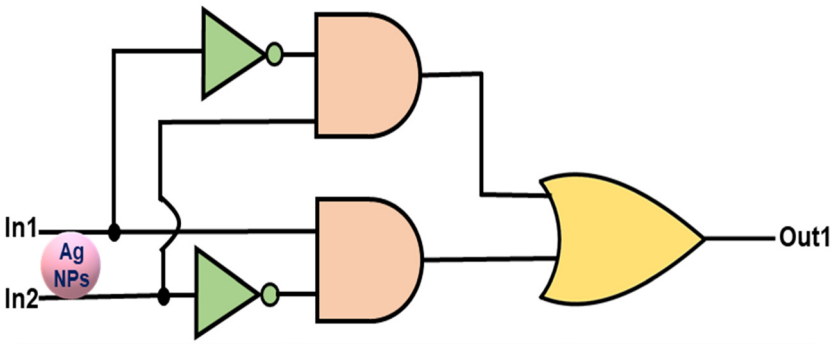

In1 (L-Cys)	In2 (D-Cys)	Out1 (CD Intensity)
False	False	False
False	True	True
True	False	True
True	True	False

Fig. 5 Expression of an XOR logic circuit diagram, and the corresponding truth table. True and False indicate the presence or absence of input. Similarly, True and False imply detectable and undetectable CD signals recorded. 5 mM of L, D-Cys were considered for the recording of the CD signals used for logic gate implementation (threshold values: ±20 (mdeg)).

NPs ('00' input), or L-Cys alone ('01'), D-Cyst alone ('10'), or combined L-Cys + D-Cys ('11') added to Ag NPs. The threshold values for the CD signals at this particular concentration was set at ±20 (mdeg) and recorded at 260 nm. The corresponding output produces XOR logic functions following the equation

$$Y = A \oplus B = \bar{A}\,B + A\,\bar{B}$$

where, A = In1 = L-Cys and B = In2 = D-Cys. The overall results mimic Exclusive OR (XOR) logic circuit, and the truth table is shown in Fig. 5.

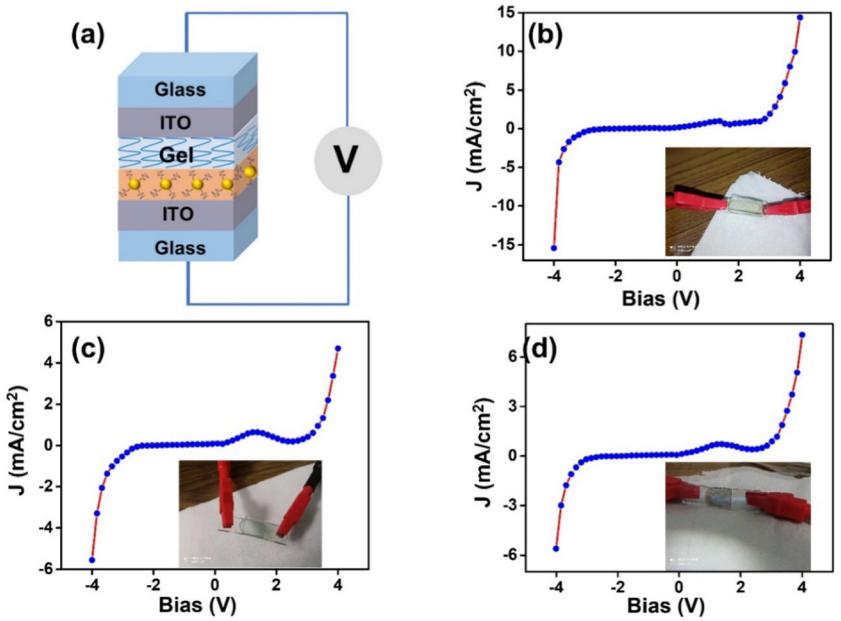

Fig. 6 (a) Schematic representation of device fabrication for *I*–*V* measurements, (b)–(d) applied voltage *vs.* current density plots of Ag NPs, L-Cys@Ag, and D-Cys@Ag NPs, respectively. Inset images show photographs of actual devices.

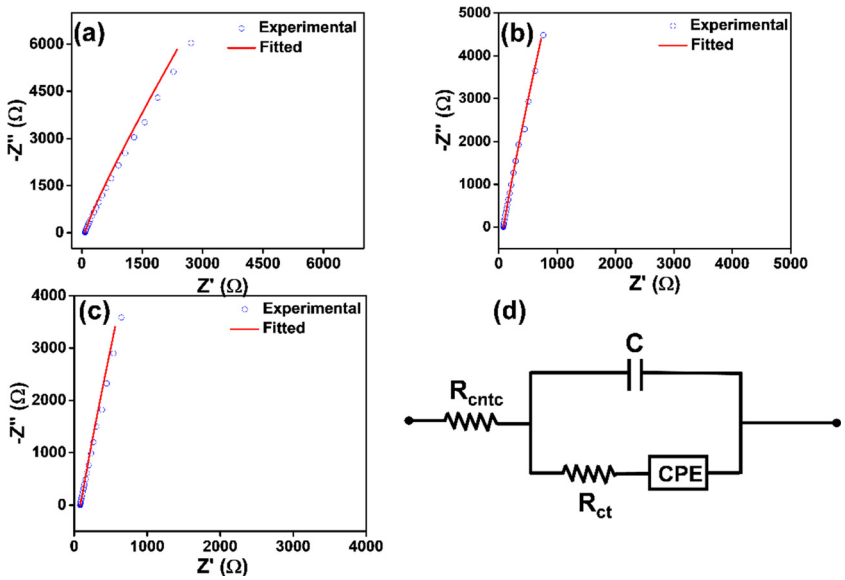

Fig. 7 (a)–(c) Nyquist plots of Ag NPs, L-Cys@Ag, and D-Cys@Ag NPs, respectively and (b) schematic fitted circuit model.

DC-based electrical characterization

Solid-state devices for electrical measurements were fabricated by combining two freshly cleaned ITO substrates. The bottom ITO-electrode (working electrode) was prepared by drop-casting the colloidal solution of Ag NPs, L-Cys@Ag, and D-Cys@Ag NPs, and an electrolyte gel was placed on another ITO, which worked as a top electrode (counter electrode). After drying at room temperature, both the ITO electrodes were combined to complete the device (Fig. 6(a)). A two-probe contact method was employed for current–voltage (I–V) measurements in these devices. A DC potential window was set between −4 V to +4 V and equal current density at the both the applied bias of 14.4 ± 0.9 mA cm^{-2} was observed for AgNPs-based devices. The current densities measured for L-Cys@Ag and D-Cys@Ag NPs was 4.7 ± 0.5 mA cm^{-2} and 5.7 ± 0.9 mA cm^{-2}, respectively (Fig. 6(b) and (c)), which are almost five times lower than that of Ag NPs. Since free Ag NPs are much more conductive, L/D-Cys are insulating; thus, the conductivity of the combined systems reduced. A little hump at about 1.27 V is observed in all three cases, which may be due to the moisture contribution. A reference device was also made with only ITO and ITO with gel, which showed completely ohmic behavior (Fig. S8, ESI†). The current density in the case of D-Cys@Ag NPs was slightly higher than in L-Cys@Ag NPs, which is according to the functionalization of Ag NPs by D-Cys, well-correlated with the previous characterization. The functionalization of Ag NPs by D-Cys was less as compared to L-Cys, which can be seen in the TEM images discussed earlier.

AC-based electrical characterization

Electrical impedance spectroscopy helps understand the discrete electrical parameters of electronic devices, which cannot be obtained from DC-based measurements.[53] Solid-state electrical impedance measurements were performed for a better understanding of the individual circuit element of the devices shown above. The AC-based experimental data were fitted using the modified Randles equivalent circuit model (Fig. 7(a)) and values of R_{cntc}, R_{ct}, C, and CPE are listed in Table S3 (ESI†). In circuit modelling, double layer capacitance is in parallel with R_{ct} and CPE ($Z^{CPE} = 1/Q(i\omega)\alpha$, a is the CPE exponent, whose value lies partitioning between 0 and 1 and the CPE parameter Q).[53] The Nyquist plot shows the charge-transfer resistance at the molecules–electrolyte and electrolyte–electrode interfaces of the devices (Fig. 7(b)–(d)). At higher frequency regime, a sharp increase in the impedance value was observed. The charge transfer resistance R_{ct} in the case of Ag NPs, L-Cys@Ag, and D-Cys@Ag NPs was 57.1 ± 0.5 Ω, 341.2 ± 1.2 Ω, and 203.4 ± 0.3 Ω, respectively. These results also show that as the functionalization occurs at the surface of Ag NPs, R_{ct} also increases; however, it also depends on the degree of functionalization. For instance, R_{ct} increased more for L-Cys@Ag NPs than for D-Cys@Ag NPs, indicating that the number of L-Cys attached to AgNPs is much higher than the D-Cys attachment. The electrical measurement indicated that the chiroptical and electrical properties of the Ag NPs depend on the degree of functionalization by chiral inducers.

3. Conclusion

Chiral ligands have been found to be a strong influence in 'copy and paste' chirality in achiral Ag NPs. Chiral amino acids contain many functional groups such as $–NH_2$, –OH, and –COOH; however, thiols are more effectively adsorbed on achiral Ag NPS surfaces over other functionalities. The formation of chiral assemblies by direct covalent bonding of Ag–S (–S from chiral ligand) can be attributed to the origin of the chiroptical property in L-Cys@Ag and D-Cys@Ag NPs, which is due to electric field polarization. The chiral ligands used here are not only able to transfer the chirality but also control the

agglomeration formation. Solution-processable L/D Cys Ag NPs were integrated into electronic devices for DC- and AC-based electrical measurements. DC-based electrical conductivity decreases in the case of surface modification of the Ag NPs with the chiral inducers, which is due to the insulating nature of chiral ligands. Thus, AgNPs alone may be a good candidate for electrical devices requiring higher conductivity; however, it is challenging to retain their metallic state. It is well-studied that Ag NPs are prone to oxidation at ambient conditions and/or agglomeration formation. The present work showcases an easy way of imprinting chirality in achiral metallic nanoparticles for tuning electrical and optical properties that may be suitable for fabricating optoelectronics and bio-applications using induced chiral nanomaterials.

Experimental section

Materials

Silver nitrate ($AgNO_3$, 99.0%), Trisodium citrate (TSC, 99%), sodium borohydride ($NaBH_4$, >96%) L-cysteine (>97%), and D-cysteine (>99%) were acquired from Sigma-Aldrich and used without any further purification.

Instrumentation used for measurements

The FTIR spectra were obtained with the help of a Bruker Alpha-II in the ATR mode in the range of 500–4000 cm^{-1}. UV-vis spectroscopy measurements were done using a JASCO UV-Visible-NIR V-770 spectrophotometer. A Carl Zeiss ULTRA Plus field emission scanning electron microscope working at 15 kV was employed for the morphological analysis. The colloidal solution was sonicated for 10 min, drop-casted on a glass substrate, and dried in vacuum overnight. The TEM study was performed by an FEI Tecnai G2 12-TWIN electron microscope operating at an acceleration voltage of 120 kV. 20 μL colloidal solution was put on carbon-coated TEM grid, which was further dried in a desiccator. The crystalline nature of the samples was analyzed by selected area electron diffraction (SAED). UV-vis analysis was performed on a JASCO V-770 in the wavelength range of 300–800 nm. The DLS size and zeta potential was measured by a Scopals PALS. The CD spectra were measured on a JASCO 815 spectrometer. The X-ray photoelectron spectra (XPS) of the synthesized colloidal nanoparticles were recorded using a PHI 5000 Versa Probe II. Current–voltage (*I–V*) measurements were performed on a Keithley Source meter 2604B. EIS and circuit modeling of the devices were studied using a GAMRY Reference 600+ Potentiostat.

Ag nanoparticles synthesis

Ag nanoparticles were synthesized by the direct reduction of silver nitrate using sodium borohydride. Typically, 20 mL of 1% solution trisodium citrate (TSC) was added to 200 mL of 5 mM $AgNO_3$ while stirring, and the temperature was maintained 60 °C. After 20 min, 20 mL of 30 mM $NaBH_4$ was added, and a pale yellow was observed, indicating the formation of silver nanoparticles. Then, 400 mg PVP K-30 was added as a surfactant into the reaction.[54] The pH of the solution was maintained at ~7.0 throughout the reaction. After 3 h of stirring the reaction mixture, a colloidal solution was collected after centrifugation and washed with distilled water several times to remove excess of surfactant and tri-sodium citrate.

Chiral modification by L/D-cysteine

200 μL of L- and D-cysteine chiral ligand with different concentrations (0.1, 0.5, 1, 5, 10 mM) were dropped into 2 mL Ag NPs colloidal solution and 1.8 mL of distilled water in a 15 mL vial;[40] the reaction was stirred at 450 rpm at room temperature for 6 h, maintaining the pH between 3 and 4. The obtained L-cysteine-capped Ag NPs (L-Cys@Ag) and D-cysteine-capped AgNPs (D-Cys@Ag) were stored at 4 °C for further studies. A schematic overview encompassing the synthetic methodology of chiral Ag NPs is illustrated in Fig. S8 (ESI†).

Fabrication of electrical devices

Indium tin oxide (ITO)-coated glasses were cleaned with *n*-hexane, acetonitrile, and isopropanol by sonicating ITO for 15 min each. Subsequently, ITO substrates were dried under N_2 flow. 1 mL of colloidal solution of Ag, L-Cys@Ag, and D-Cys@Ag nanoparticles were drop-casted on cleaned ITO and dried at room temperature in a desiccator. Another ITO coated with a gel electrolyte was used to contact the NPs-deposited ITO for electrical measurements at ambient conditions.

Author contributions

PCM: conceptualization; funding acquisition; investigation; supervision; writing – original draft. MM: experiment; writing – original draft. AM: writing – review & editing.

Conflicts of interest

There are no conflicts to declare.

Acknowledgements

MM, and AM acknowledges IIT Kanpur (IITK/CHM/2019044) for a junior research fellowship, and post-doctoral fellowship, respectively. PCM acknowledges a research grant from the Department of Science and Technology (EEQ/2019/000708), New Delhi.

References

1 S. Ghosh and L. Manna, *Chem. Rev.*, 2018, **118**, 7804–7864.
2 K. Saha, S. S. Agasti, C. Kim, X. Li and V. M. Rotello, *Chem. Rev.*, 2012, **112**, 2739–2779.
3 J. Zhang, L. Zhong, Y. Sun, A. Li, J. Huang, F. Meng, B. K. Chandran, S. Li, L. Jiang and X. Chen, *Adv. Mater.*, 2016, **28**, 2978–2982.
4 S. D. Perrault and W. C. W. Chan, *J. Am. Chem. Soc.*, 2009, **131**, 17042–17043.

5 E. C. Dreaden, A. M. Alkilany, X. Huang, C. J. Murphy and M. A. El-Sayed, *Chem. Soc. Rev.*, 2012, **41**, 2740–2779.
6 G. Cao, *Nanostructures and nanomaterials – Synthesis, Properties and Applications*, Imperial College Press, London, 2004.
7 S. Eustis and M. A. El-Sayed, *Chem. Soc. Rev.*, 2006, **35**, 209–217.
8 I. E. Santizo, F. Hidalgo, L. A. Pérez, C. Noguez and I. L. Garzón, *J. Phys. Chem. C*, 2008, **112**, 17533–17539.
9 S. M. Mullins, H. C. Weissker, R. Sinha-Roy, J. J. Pelayo, I. L. Garzón, R. L. Whetten and X. López-Lozano, *Nat. Commun.*, 2018, **9**, 3352.
10 C. Noguez and I. L. Garzón, *Chem. Soc. Rev.*, 2009, **38**, 757.
11 R. L. Whetten, H. C. Weissker, J. J. Pelayo, S. M. Mullins, X. López-Lozano and I. L. Garzón, *Acc. Chem. Res.*, 2019, **52**, 34–43.
12 J. M. Abendroth, D. M. Stemer, B. P. Bloom, P. Roy, R. Naaman, D. H. Waldeck, P. S. Weiss and P. C. Mondal, *ACS Nano*, 2019, **13**, 4928–4946.
13 P. C. Mondal, C. Fontanesi, D. H. Waldeck and R. Naaman, *ACS Nano*, 2015, **9**, 3377–3384.
14 A.-M. Guo and Q. Sun, *Phys. Rev. Lett.*, 2012, **108**, 218102.
15 R. Rodríguez, C. Naranjo, A. Kumar, P. Matozzo, T. K. Das, Q. Zhu, N. Vanthuyne, R. Gómez, R. Naaman, L. Sánchez and J. Crassous, *J. Am. Chem. Soc.*, 2022, **144**, 7709–7719.
16 S. Tsunega, T. Tanabe and R. H. Jin, *Nanoscale Adv.*, 2019, **1**, 581–591.
17 A. Guerrero-Martínez, J. L. Alonso-Gómez, B. Auguié, M. M. Cid and L. M. Liz-Marzán, *Nano Today*, 2011, **6**, 381–400.
18 H.-E. Lee, H.-Y. Ahn, J. Mun, Y. Y. Lee, M. Kim, N. H. Cho, K. Chang, W. S. Kim, J. Rho and K. T. Nam, *Nature*, 2018, **556**, 360–365.
19 H. Kim, S. W. Im, N. H. Cho, D. H. Seo, R. M. Kim, Y.-C. Lim, H.-E. Lee, H.-Y. Ahn and K. T. Nam, *Angew. Chem., Int. Ed.*, 2020, **59**, 12976.
20 W. Ma, L. Xu, A. F. de Moura, X. Wu, H. Kuang, C. Xu and N. A. Kotov, *Chem. Rev.*, 2017, **117**, 8041–8093.
21 N. A. Kotov, L. M. Liz-Marzán and P. S. Weiss, *ACS Nano*, 2021, **15**, 12457–12460.
22 M. Sujith, E. K. Vishnu, S. Sappati, M. S. Oliyantakath Hassan, V. Vijayan and K. G. Thomas, *J. Am. Chem. Soc.*, 2022, **144**, 5074–5086.
23 J. Mosquera, Y. Zhao, H. Jang, N. Xie, C. Xu, N. A. Kotov and L. M. Liz-Marzán, *Adv. Funct. Mater.*, 2020, **30**, 1902082.
24 K. T. Nam and H. Kim, *Science*, 2021, **371**, 1311.
25 J. Lv, X. Gao, B. Han, Y. Zhu, K. Hou and Z. Tang, *Nat. Rev. Chem.*, 2022, **6**, 125–145.
26 P. C. Mondal, D. Asthana, R. K. Parashar and S. Jadhav, *Mater. Adv.*, 2021, **2**, 7620–7637.
27 A. Sánchez-Castillo, C. Noguez and I. L. Garzón, *J. Am. Chem. Soc.*, 2010, **132**, 1504–1505.
28 G. Zheng, J. He, V. Kumar, S. Wang, I. Pastoriza-Santos, J. Pérez-Juste, L. M. Liz-Marzán and K. Y. Wong, *Chem. Soc. Rev.*, 2021, **50**, 3738–3754.
29 D. Vila-Liarte, N. A. Kotov and L. M. Liz-Marzán, *Chem. Sci.*, 2022, **13**, 595–610.
30 K. H. Park, J. Kwon, U. Jeong, J. Y. Kim, N. A. Kotov and J. Yeom, *ACS Nano*, 2021, **15**, 15229–15237.
31 J. Y. Kim, J. Yeom, G. Zhao, H. Calcaterra, J. Munn, P. Zhang and N. Kotov, *J. Am. Chem. Soc.*, 2019, **141**, 11739–11744.
32 L. Ma, Z. Huang, Y. Duan, X. Shen and S. Che, *Sci. China Mater.*, 2015, **58**, 441–446.
33 R. L. Whetten, H. C. Weissker, J. J. Pelayo, S. M. Mullins, X. López-Lozano and I. L. Garzón, *Acc. Chem. Res.*, 2019, **52**, 34–43.
34 T. Gregory Schaaff and R. L. Whetten, *J. Phys. Chem. B*, 2000, **104**, 2630–2641.
35 N. N. Zhang, H. R. Sun, Y. Xue, F. Peng and K. Liu, *J. Phys. Chem. C*, 2021, **125**, 10708–10715.
36 C. Gautier and T. Bürgi, *ChemPhysChem*, 2009, **10**, 483–492.
37 N. H. Cho, G. H. Byun, Y.-C. Lim, S. W. Im, H. Kim, H.-E. Lee, H.-Y. Ahn and K. T. Nam, *ACS Nano*, 2020, **14**, 3595–3602.
38 J. J. Pelayo, R. L. Whetten and I. L. Garzón, *J. Phys. Chem. C*, 2015, **119**, 28666–28678.
39 R. Gupta, P. Jash and P. C. Mondal, *J. Mater. Chem. C*, 2021, **9**, 11497–11516.
40 J. Wang, S.-S. Zhang, X. Xu, K.-X. Fei and Y.-X. Peng, *Nanomaterials*, 2018, **8**, 1027.
41 M. Jakob, A. Von Weber, A. Kartouzian and U. Heiz, *Phys. Chem. Chem. Phys.*, 2018, **20**, 20347–20351.
42 P. Rodríguez-Zamora, C. A. Cordero-Silis, G. R. Garza-Ramos, B. Salazar-Angeles, J. C. Luque-Ceballos, J. C. Fabila, F. Buendía, L. O. Paz-Borbón, G. Díaz and I. L. Garzón, *Small*, 2021, **17**, 2004288.
43 J. Nan and X.-P. Yan, *Chem. – Eur. J.*, 2010, **16**, 423–427.
44 A. Stewart, S. Murray and S. E. J. Bell, *Analyst*, 2015, **140**, 2988–2994.
45 A. Obaid, A. K. Mohd Jamil, S. M. Saharin and S. Mohamad, *Chirality*, 2021, **33**, 810–823.
46 C. Garrido, A. E. Aliaga, J. S. Gómez-Jeria, J. J. Cárcamo, E. Clavijo and M. M. Campos-Vallette, *Vib. Spectrosc.*, 2012, **61**, 94–98.
47 A. Malik and M. Nath, *J. Environ. Chem. Eng.*, 2020, **8**, 104547.
48 L. Rosenfeld, *Z. Phys.*, 1929, **52**, 161–174.
49 B. Janani, A. Syed, A. M. Thomas, N. Marraiki, S. Al-Rashed, A. M. Elgorban, L. L. Raju, A. Das and S. S. Khan, *J. Mol. Liq.*, 2020, **311**, 113281.
50 J. M. Slocik, A. O. Govorov and R. R. Naik, *Nano Lett.*, 2011, **11**, 701–705.
51 J. Guan, J. E. Park, S. Deng, M. J. H. Tan, J. Hu and T. W. Odom, *Chem. Rev.*, 2022, **122**, 15177–15203.
52 B. M. Maoz, R. van der Weegen, Z. Fan, A. O. Govorov, G. Ellestad, N. Berova, E. W. Meijer and G. Markovich, *J. Am. Chem. Soc.*, 2012, **134**, 17807–17813.
53 R. Gupta, P. Jash, A. Pritam and P. C. Mondal, *Can. J. Chem.*, 2022, **8**, 1–8.
54 D. R. Bae, W. S. Han, J. M. Lim, S. Kang, J. Y. Lee, D. Kang and J. H. Jung, *Langmuir*, 2010, **26**, 2181–2185.